PROCEEDINGS, 51st Workshop on Geothermal Reservoir Engineering
Stanford University, Stanford, California, February 9-11, 2026
SGP-TR-230

Fluid Injection-Induced Fracture Evolution and Breakdown Pressure in Naturally Fractured Rocks with Ultra-Low Permeability Matrix

Shivesh Shandilaya[1] and Shahrzad Roshankhah[1*]

[1]Civil and Environmental Engineering, University of Utah, Salt Lake City, Utah, USA

[*]Shahrzad.Roshankhah@utah.edu

Keywords: Enhanced Geothermal Systems, Breakdown Pressure, FED-DEM Simulations, HF-NF interactions, Rock Block Interlocking.

ABSTRACT

The energy geosystems that involve fluid injection into geological formations, such as shale oil and gas and enhanced geothermal systems (EGS), are increasing in number and importance every day. To improve efficiency and ensure the sustainability of these geosystems, one must understand the mechanisms and factors that govern the evolution of the induced fracture network in naturally fractured ultra-low-permeability rock masses. Previous studies have demonstrated that natural fracture characteristics strongly influence both the hydraulic and mechanical responses of such formations. In this study, a combined finite–discrete element method (FDEM) is employed to investigate coupled hydromechanical processes during fluid injection, with particular emphasis on the role of natural fracture (NF) density. The results show that NF density significantly influences near-wellbore fracture initiation behavior controlling the breakdown pressure as the NF density increases. Following fracture propagation and crossing of NFs, fluid pressure dissipates along preferential pathways through the viscous drag process, thereby limiting the energy available to create new fractures. We hypothesize that increasing NF density amplifies lateral stress around the wellbore due to rock block interlocking, which leads to higher rock mass shear strength mobilization at lower shear displacements (Barton, et al., 1985). Understanding these phenomena will provide insights into implementing effective strategies for safer, more sustainable fluid injection practices in EGS.

1. INTRODUCTION

Enhanced geothermal systems (EGS) are crucial in diversifying the energy mix and achieving a net-zero carbon energy economy. This geo-energy application involves high-rate water injection to form an extensive network of fractures, including hydraulic fractures (HFs) and activated pre-existing natural fractures (NFs), in geological formations with ultra-low permeability matrices traversed by non-persistent, often cemented NFs. Research shows that geological factors, such as the direction, magnitude, and degree of anisotropy of the in-situ principal stresses relative to the orientation of dominant NFs, and hydro-mechanical properties of NFs and the rock matrix, contribute significantly to the overall hydromechanical behavior of the rock mass (Wasantha et al., 2019; Zeng et al., 2020). In a homogeneous and isotropic material under anisotropic stresses, high-rate fluid injection induces hydraulic fractures parallel to the maximum principal stress. Under an isotropic stress condition, HFs branch and propagate in many directions. However, isotropic stress has not been observed in the depth range of active energy geosystems. For example, the stress state at the Utah Forge site at a depth of about 10,000 ft is reported as σ_v = 62 MPa and $\sigma_{H,\,max}$ = 48 MPa (Xing et al., 2022). Thus, the fracture network complexity can be influenced by NF characteristics, rock matrix, fluid properties, and operational parameters, such as the injection rate.

Interactions between HFs and NFs must be understood under various conditions. There have been many laboratory and numerical studies on interactions between HFs and a single NF. Several possible interaction scenarios between HF and a single NF are identified. For example, the hydraulic fracture will likely cross an NF if the HF approaches the NF with a high angle (e.g., close to 90◦), far-field stress anisotropy is high, or the NF is strongly bonded/cemented. If the HF approaches the NF with a low angle (e.g., 20◦), far-field stress anisotropy is low, or the NF is unbonded/open, HF penetrates through the NF, activating/dilating it. The HF may then resume propagating from farther along the NF with an offset, or the NF may propagate from one or both sides, depending upon the in-situ stress state, NFs frictional strength, and available pressure through continued injection (e.g., Cheng et al., 2015; Daneshy et al., 2019; Kolawole et al., 2020; Chen et al., 2021; Zhao et al., 2023).

The first hypothesis in this study is that the interactions between an HF and the NF network differ from those between an HF and a single NF when the NFs are closer together than the medium's characteristic length. The characteristic length of the medium depends on the characteristics of NFs (geometric and hydro-mechanical properties), the hydro-mechanical properties of the rock matrix, fluid properties, and operational parameters. In low-density naturally fractured media, HF-NF interactions approach those observed between an HF and a single NF. In heavily fractured media, HF behavior approaches that in a statistically homogeneous discrete area. In moderately fractured media, the collective effects of the NF network define the overall hydro-mechanical behavior of the media. Moderate NF density increases the likelihood of HF deflection and interactions with multiple NFs, leading to more complex fracture growth and larger SRV. Previous research posits that randomly orientated NFs with moderate density promote the development of shear and tensile cracks along multiple NFs, while reducing tensile cracking in the rock matrix. Shear cracks in the matrix, however, remain largely unaffected, reflecting a shift from single-fracture to network-controlled hydromechanical behaviour (Chong et al., 2017).

Considerable effort has been devoted to numerical investigations of fluid-injection-induced fracture evolution in a naturally fractured medium, focusing on NF characteristics, rock matrix properties, and stress regimes. Previous numerical studies have been using the

continuum-based, finite element methods (FEM) (e.g., Lecampion, 2009; Chen et al., 2017), the discontinuum-based, discrete/distinct element methods (DEM) (e.g., Huang et al., 2019; Kwok et al., 2020), or the combined FEM-DEM (Yan et al., 2016; Zheng et al., 2020). One of the limitations of FEM is that when applied to problems involving large deformations like fracturing, it faces challenges like mesh distortion, making it less effective for accurately capturing the fracture due to the stress singularity at the fracture tip (Wangen, 2013; Li et al., 2021; Yan et al., 2022). The extended finite element method (XFEM) has been developed to overcome those challenges (Belytschko & Black, 1999), but its application suffers from overly complicated functions and many non-physical parameters, which make model calibration and validation difficult (Spencer et al., 2014). DEM is associated with a predefined fracture-propagation path among rigid rock blocks and has a high computational cost due to the tracking of discrete bodies (Gerekova et al., 2020). The bonded particle method (BPM) has been extended from DEM to enable fracture formation on any path required by the boundary and loading conditions, including through the rock blocks. This capability, however, makes the analysis even more computationally intensive because it requires tracking all particles that comprise the rock blocks (Potyondy and Cundall, 2004).

The numerical analysis method employed in this study is the combined finite-discrete element method (FDEM), implemented in Irazu (Geomechanica Inc., 2024). FDEM leverages the strengths of FEM, such as lower computational cost, and those of DEM, where discontinuous bodies can interact with one another in any manner required by boundary and loading conditions. The hybrid FDEM technique enables modeling the transition of a semi-continuum medium (i.e., a naturally fractured rock with dormant NFs) to a semi-discrete medium (i.e., a rock mass with an activated fracture network). FDEM can help researchers understand the effects of new fracture initiation, propagation, and interactions with pre-existing NFs on the hydro-mechanical behavior of geological materials (Lisjak et al., 2016; Wu et al., 2021; Yan et al., 2022).

2. MATHEMATICAL FORMULATION

The FDEM formulation (Munjiza et al., 1995) is used to model four fluid injection cases in this study. Mathematical formulation and verification of the mechanical processes utilised in this program are published in several articles and reports (Munjiza et al., 1995; Munjiza & Andrews, 1998; Mahabadi et al., 2012; Tatone & Grasselli, 2015; Lisjack et al., 2017; Geomechanica, 2024; Shandilaya & Roshankhah, 2025). This study performs hydromechanical coupling, in which the mechanical response of the rock mass and the fluid flow within fractures and porous elements are solved fully coupled. The fluid domain interacts directly with the deformable solid elements, enabling simulation of stress redistribution due to fluid pressure, fracture initiation and propagation, and leak-off into the surrounding matrix. Once contact forces are calculated from the mechanical processes, fluid pressure forces are determined by assuming that flow occurs only through the flow channels coinciding with the crack elements and the virtual cavities at the nodes of the finite elements, as shown in Figure 1a. The volume of fluid stored within each virtual cavity is determined from the mechanically evolving fracture aperture. For each joint *j*, the local cavity volume contribution is defined as half of the joint volume, i.e., $\frac{V_j}{2}$, assigned by each cavity, where V_j is the product of the average aperture at the two ends of the flow channel, i.e., a_0 and a_1, the length of the joint, L_j (m), and a unit depth.

$$V_{cavity} = \sum_j L_j \frac{a_0 + a_1}{2} \tag{1}$$

Now, the initial fluid mass stored within each cavity, m^{t_0} (kg) is computed, assuming a linear compressibility model for the fluid, having S^{t0} as the initial cavity saturation, ρ_f (kg/m^3) as the fluid density, P^{t0} as the initial cavity pressure (Pa), and K_f (Pa) as the bulk modulus of the fluid as

$$m^{t_0} = S^{t_0} V_c \rho_f \left(1 + \frac{P^{t_0}}{K_f}\right) \tag{2}$$

The volumetric flow rate per unit length, q (m^3/s/m) in the flow channels as shown in Figure 1b, is given below according to darcy's law in terms of u_0 and u_1 (Pa) as the fluid pressures at the two ends of a flow channel, fluid density, ρ_f (kg/m3), and flow resistance (inverse of hydraulic conductivity), R (s/m), gravitational acceleration, g (m/s2), and fluid saturation of the cavity, S.

$$q = \frac{dm}{dt} = -\frac{u_1 - u_0 + \rho_f g(y_1 - y_0)}{R} \tag{3}$$

Where y_1 and y_0 are the elevations of the cavity at both ends of the flow channel. This can be written using the forward Euler method:

$$\Delta m_0 = \Delta m_1 = f(S) \frac{u_1 - u_0 + \rho_f g(y_1 - y_0)}{R} \Delta t_h \tag{4}$$

$$f(S) = S^2(3 - 2S) \tag{5}$$

The fluid pressure force is then calculated using the change in mass at each hydraulic timestep. The change in mass is given by the flow resistance, which is calculated assuming flow through parallel plates and using the cubic law, kinematic viscosity, υ (m^2/s) of the fluid, hydraulic aperture, a (m), and the length of the flow channel, L (m) as

$$R = \frac{12\upsilon}{a^3} L = 12\upsilon \int_{x_1}^{x_0} \frac{1}{a(x)^3} dx = \frac{6\upsilon(a_0 + a_1)}{(a_0 a_1)^2} L \tag{6}$$

$$P^t = \begin{cases} P^{t-1} + K_f \frac{\Delta m}{\rho_f V_{cavity}^t} & if\ S^t = 1 \\ 0 & if\ 0 \le S^t < 1 \end{cases} \tag{7}$$

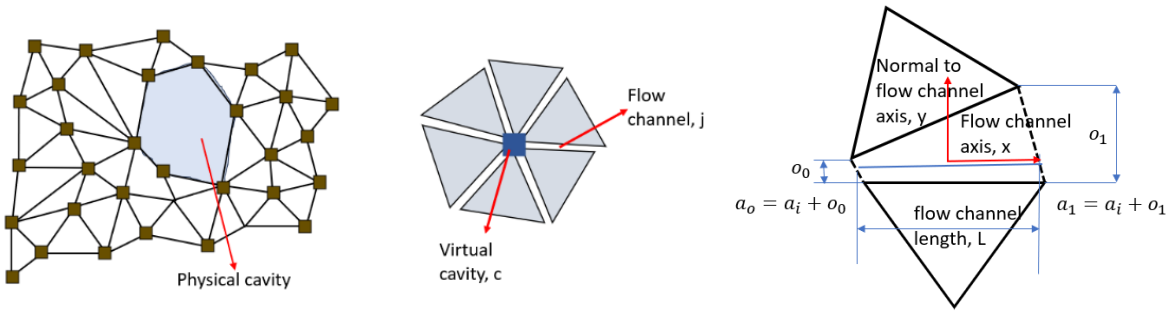

(a) (b)

Figure 1: Schematics of the FDEM hydraulic solver's components (a) Virtual cavities at elemental nodes are connected through flow channels. Physical cavities, such as a well-bore, can also be explicitly modeled. (b) Fow channel geometry between two cavities and hydraulic aperture calculation, and definitions of the flow channel and normal axes (after Lisjak et al., 2017).

3. CALIBRATION OF MODEL PARAMETERS

The calibration of input parameters is crucial for maintaining the accuracy, standardisation, scalability, and repeatability of results in any numerical simulation. By comparing numerical results with classic analytical formulation, the approach outlined in this section ensures reliability and conforms to conventional calibration procedures (Roshankhah et al., 2020). The calibration process for this study begins with selecting granite material properties from laboratory testing reported in a Utah FORGE lab characterization study (McLennan et al., 2022). Using these properties, the numerical model's parameters are first calibrated in the elastic regime by adjusting the normal and tangential penalty coefficients to reproduce the analytical Kirsch solution for stresses around a circular borehole. This step ensures that the near-wellbore stress concentration and pressure transfer are accurately captured prior to fracture initiation. Figure 2a shows the two-dimensional (2D) model geometry and boundary conditions used to verify the Kirsch analytical solution. The same domain size and mesh configuration are used in the calibration models as those in this study's models. The mesh includes a refined mesh size of 0.1 m around the wellbore and a coarser mesh size of 2 m near the domain boundaries. The model input parameters are listed in Table 1. The parameters for the crack elements shown here represent the granite rock matrix. Fracture, normal, and tangential penalty coefficients are varied until σ_r and σ_θ around a pressurized cavity in a 200 m × 200 m domain match the Kirsch analytical solution. As shown in Figure 2b, $p_n = p_t = p_f$ = 11,000 GPa·m or GPa/m achieves the match between the two methods.

Following calibration of the penalty coefficients in the elastic regime, the same geometry is subsequently employed to verify the hydraulic fracture response. The model is subjected to fluid injection along the wellbore wall, which induces tensile fractures from both top and bottom of the borehole due to the concentrated tangential stresses at those points, as shown in Figure 3a. The fracture energy, G_{Ic} (J/m^2) is calibrated by matching the numerically predicted breakdown pressure with the analytical breakdown pressure obtained from the Kirsch-based hoop stress criterion. The mode-I fracture energy, G_{II-c} =50 J/m^2, and mode-II fracture energy, G_{II-c} =500 J/m^2, reproduce the analytical breakdown pressure, resulting in a peak wellbore pressure of approximately 92 MPa (Hubbert & Willis, 1957), followed by a sharp pressure drop to the initial reservoir pressure of 24 MPa, as shown in Figure 3b.

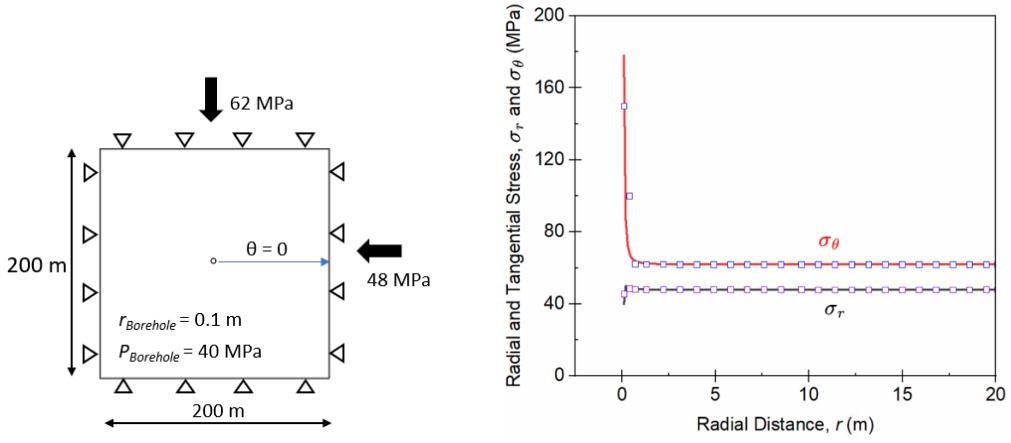

(a) (b)

Figure 2: Calibration of penalty coefficients by matching the numerically obtained stress field from Irazú with the analytical Kirsch solution around a pressurized circular cavity along $\theta = 0°$ under the specified (a) geometry and boundary conditions. (b) penalty coefficients of $p_n = p_t = p_f$ = 11,000 GPa·m yield close agreement between the numerical and analytical radial and tangential stresses away from the pressurized cavity wall.

Table 1: Mechanical, fracture, and hydraulic properties in the FDEM model for the granite rock matrix.

Element Type	Parameter	Values	References
Finite Elements	Young's Modulus, E (GPa)	55	McLennan, J. (2022)
	Poisson's Ratio, ν	0.26	McLennan, J. (2022)
	Density, ρ (kg/m^3)	2,660	McLennan, J. (2022)
Crack Elements	Tensile strength, σ_t (MPa)	10	Hoek and Brown (1980)
	Cohesion, c (MPa)	23.7	Bijay et al. (2025)
	Friction angle, ϕ (◦)	51	Bijay et al. (2025)
	Mode-I fracture energy, $G_{I\text{-}c}$ (J/m^2)	50	Matches breakdown pressure
	Mode-II fracture energy, $G_{II\text{-}c}$ (J/m^2)	500	10 x $G_{I\text{-}c}$
	Fracture penalty coefficient, p_f (GPa/m)	11,000	Matches Kirsch solution
	Normal penalty coefficient, p_n (GPa·m)	11,000	Matches Kirsch solution
	Tangential penalty coefficient, p_t (GPa/m)	11,000	Matches Kirsch solution
Flow Channels	Initial aperture, a_i (m)	1 x 10^{-5}	Geomechanica et al. (2025)
	Residual aperture, a_r (m)	1 x 10^{-5}	Geomechanica et al. (2025)
	Threshold aperture, a_t (m)	0.00043	Sensitivity analysis

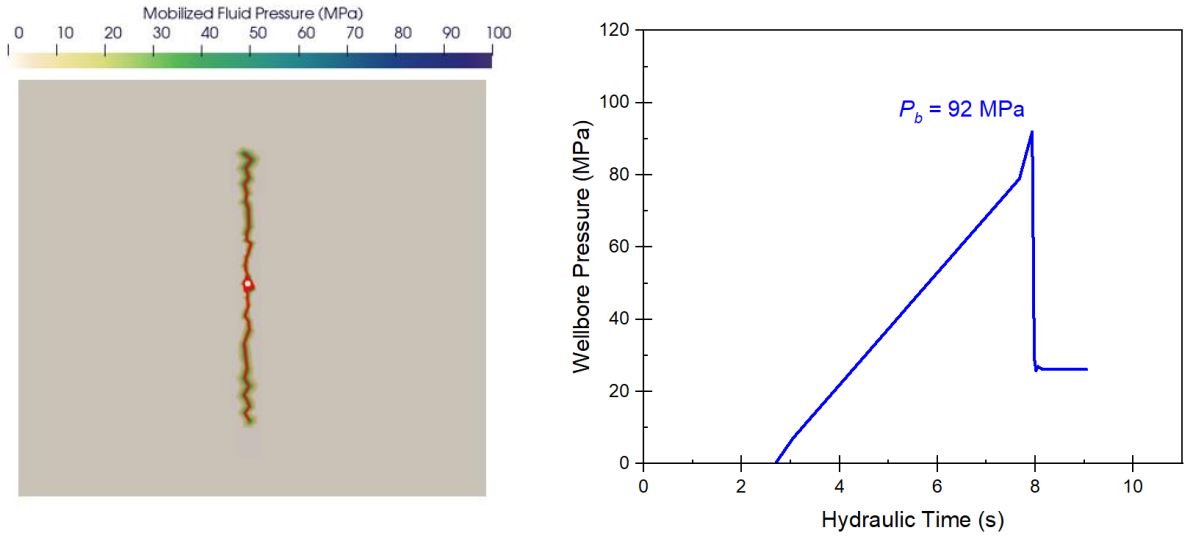

(a) (b)

Figure 3: Calibration of fracture energy of crack elements in the rock matrix. (a) Mobilized fluid pressure field superimposed on the broken joints, and (b) Wellbore pressure evolution showing a breakdown pressure of approximately 92 MPa and post fracture pressure stabilization to the reservoir pressure of 24 MPa.

4. MODEL CONFIGURATIONS

The model domain of 200 × 200 m^2 is selected to adequately represent the 91.4 m spacing between the stimulation and production wells at the Utah FORGE site (McLennan et al., 2022). Fixed displacement boundary conditions are imposed in the x and y directions on all boundaries, as shown in Figure 4.

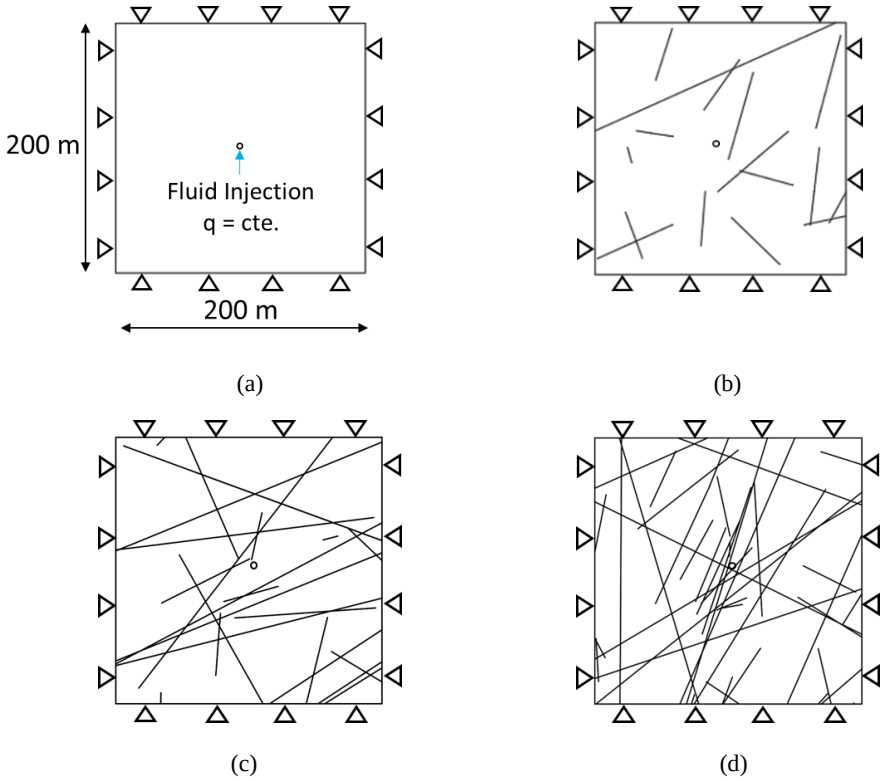

Figure 4: Model configurations used in the simulation for the water injection at the center of formations in a (a) Homogeneous medium, (b) Low-density NF, (c) Medium-density NF, and (d) High-density NF network medium, under an anisotropic stress state of σ_v=62 MPa and σ_h=48 MPa and zero displacement in the vertical and horizontal direction.

A total of four models is used in this study. The model materials under study include one homogeneous, isotropic material (Figure 4a) and three heterogeneous materials. The heterogeneous models are designed to study the effects of NF density on the hydromechanical response of a rock mass, i.e., low-density (Figure 4b), medium-density (Figure 4c), and high-density (Figure 4d) models. Natural fractures are extracted from microseismic images at the Utah Forge site, specifically from well 16-A. Two locations along the horizontal wellbore are identified, where relatively low-density DFNs and relatively high-density DFNs are present. The orientation of the extracted 2D tracemaps is near perpendicular to the horizontal wellbore. The rock matrix in all models is impermeable, mimicking the ultra-low permeability of rocks like granite in EGS. The far-field stress conditions are anisotropic, with σ_v = 62 MPa and σ_h = 48 MPa, resembling those of a Utah Forge reservoir (Xing et al., 2022).

The mechanical and hydraulic parameters of the natural fractures are listed in Table 2. Cohesion and friction angle of NFs are derived from shear strength tests on Utah FORGE granite (Bijay et al., 2025), and the tensile strength and fracture energies are computed using the Hoek–Brown and Whittaker formulations, respectively. The penalty parameters are identical to those of the rock matrix. The initial and residual apertures of NFs are assigned values one order of magnitude greater than those of the flow channels in rock matrix, and the threshold aperture is determined from a sensitivity analysis with respect to hydraulic time and artificial pressure mobilization.

The geostatic stress equilibrates with an initial 2M time steps of FEM simulation. Water with a viscosity of 2×10^{-3} Pa.s and bulk modulus of 0.44 MPa is injected at the center of the 2D model at a rate of 0.72 kg/s, corresponding to a volumetric flow rate of 0.072 m^3/s in the Utah Forge site (Xing et al., 2022). The hydraulic time for the simulation is calculated as 344 s, based on the injection volume (708.8 m^3) and the total well injection depth (2,610 m) for the Utah Forge project. The model was run for 60,000 mechanical steps before the injection process began to achieve proper elemental overlaps. The hydromechanical calculations then proceed with 19 mechanical steps for each hydraulic step to ensure stress equilibration before each hydraulic disturbance.

Table 2: Mechanical, fracture, and hydraulic properties of natural fractures (NFs) used in the FDEM model.

Parameter	Values	References
Tensile strength, σ_t (MPa)	6.22	Hoek and Brown (1980)
Joint shear strength intercept, c (MPa)	5.82	Bijay et al. (2025)
Friction angle of joint, ϕ_j (◦)	33.8	Bijay et al. (2025)

Parameter	Values	References
Mode-I fracture energy, G_{I-c} (J/m^2)	14.8	Whittaker et al. (1992)
Mode-II fracture energy, G_{II-c} (J/m^2)	148	Whittaker et al. (1992)
Fracture penalty coefficient, p_f (GPa/m)	11,000	Same as rock matrix
Normal penalty coefficient, p_n (GPa·m)	11,000	Same as rock matrix
Tangential penalty coefficient, p_t (GPa/m)	11,000	Same as rock matrix
NF initial aperture, a_i (m)	1 x 10^{-4}	$K_{NF} \gg K_{matrix}$
NF residual aperture, a_r (m)	1 x 10^{-4}	$K_{NF} \gg K_{matrix}$
NF threshold aperture, a_t (m)	1 x 10^{-3}	$K_{NF} \gg K_{matrix}$

5. RESULTS AND DISCUSSIONS

Figure 5 shows the mobilized fluid pressure in the four models superimposed on the initial NF pattern and generated broken joints due to fluid injection. The homogeneous medium shows highly localized fluid pressure around the propagating hydraulic fracture parallel to the maximum principal stress direction, as shown in Figure 5a, as expected. However, as NF density increases, as shown in Figures 5b and c for low and medium-density NF media, pressure is dissipated through the NF channels to which HF deviates and so it does not propagate to a longer distance. This is also illustrated in Figure 6, where fluid pressure along the main HF is shown, and pressure drops as HF crosses NFs. In low- and medium-density NF cases, the main hydraulic fracture crosses the first NFs that it encounters before diverting into them. This behavior is attributed to the relatively high bonding strength of natural fractures and high HF-NF approach angle. Under these conditions, NFs behave as mechanically strong interfaces that resist opening slip. Consequently, fracture propagation remains primarily governed by the far-field stress orientation rather than by HF diversion along NF planes, leading to systematic HF crossing across all NF density scenarios.

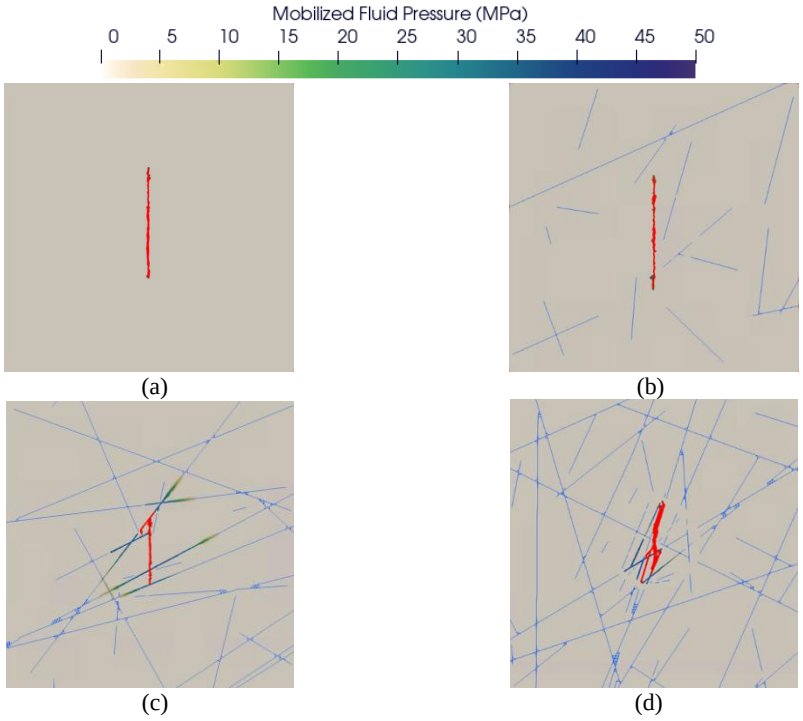

Figure 5: Mobilized fluid pressure distribution during injection superimposed on the initial natural fracture network and broken joints generated due to fluid injection in: (a) homogeneous, (b) low-density NF, (c) Medium-density NF, and (d) High-density NF media.

In contrast to the low and medium density NF cases, the fracture response in high density NF medium becomes increasingly complex, with extensive HF–NF merging, as shown in Figure 5d, which promotes channeling of the injected fluid and rapid dissipation of mobilized

fluid pressure through multiple intersecting flow paths, resulting in a pronounced and earlier pressure drop away from the wellbore, as shown in Figure 6. The hydraulic path is also found to deviate from the far-field principal stress direction due to stress redistribution during the HF-NF interactions. Far-field stress is redistributed by NFs, and as a result, shear stress acts along the hydraulic fracture path; the hydraulic fracture then propagates along a different path (Shandilaya, et al., 2026).

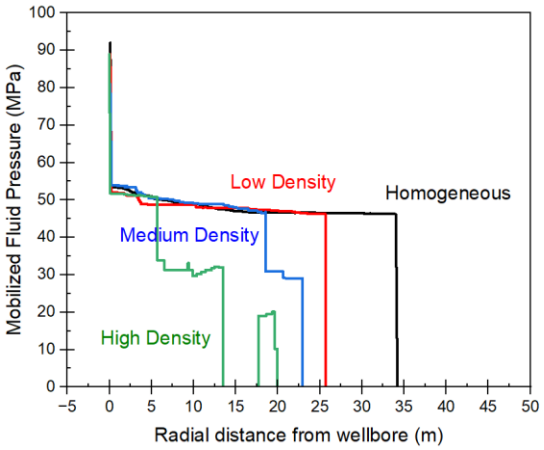

Figure 6: Mobilized fluid pressure along the radial distance from the wellbore for homogeneous and fractured media with low-density, medium-density, and high-density NF network.

Table 3 summarizes the simulation results in terms of the breakdown pressure, cumulative broken-joint length, and time to reach breakdown for all the four models in this study. The breakdown pressure obtained for the homogeneous case is validated against the analytical solution (Hubbert & Willis, 1957), providing a benchmark for assessing the influence of natural fracture density of a rock mass on its breakdown and fracture evolution behavior. The breakdown pressure decreases with increasing NF density up to the medium density NF model. This occurs because naturally fractured media are more compliant in the near-wellbore region until the NF density exceeds a threshold. However, with a further increase in the NF density, the breakdown pressure increases to the highest value among all models (Chong et al., 2017). We attribute this behavior to enhanced mechanical interlocking between the rock blocks at this NF density, which increases the shear strength and stiffness of the fractured medium (Barton, et al., 1985).

Table 3: Breakdown pressure, time to breakdown, and total length of broken joints for homogeneous and naturally fractured media of different NF density.

Case	Fracture Density, P21	Time taken to reach breakdown (s)	Broken Joint length (m)	Breakdown Pressure (MPa)
Homogenous	0	7.94	68.04	92
Low-Density NF	0.02	7.37	51.32	89
Medium-Density NF	0.06	6.93	49.60	81
High-Density NF	0.09	8.05	65.06	98

The temporal evolution of broken joints' length and failure mode are shown in Figure 7 for all models. As shown in Figure 7a, the homogeneous model indicates that fracture propagation is primarily driven by tensile failure in the rock matrix, as expected and reported in various literature (Chong et al., 2017; Shi et al., 2023). A few clack elements broke through shear as well, which is likely due to the inclined crack elements relative to the local stresses driving fractures leading to shear or mixed-mode damage. With the introduction of NFs (Figure 7b), the number of joints breaking in tensile mode decrease due to enhanced stress relaxation and earlier breakdown, which suppresses tensile opening and limits elastic energy accumulation. Fracture propagation in the tensile mode further decreases with increasing NF density (Figure 7c). However, fracture propagation under shear mode is found to increase with increasing NF density, especially NFs failing in shear (Figure 7c and d). This can happen because of increased interlocking between the rock blocks.

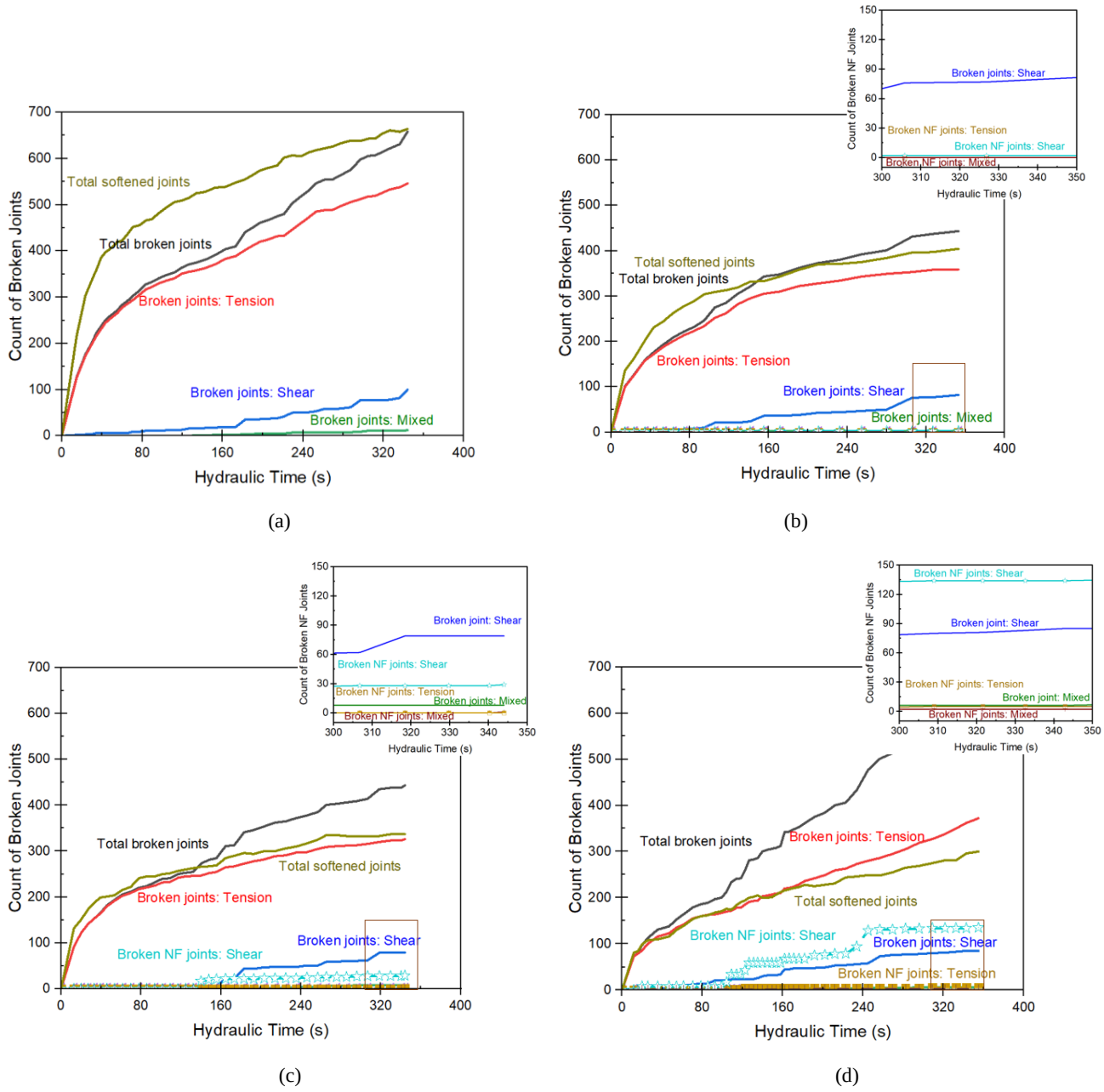

Figure 7: Temporal evolution of broken joints in the rock matrix and NF network for: (a) homogeneous, (b) low-density NF, (c) Medium-density NF, and (d) High-density NF media.

These results show that the reason for the increase in the breakdown pressure in the high-density NF model may be the increased rock block interlocking, which leads to an increased shear-dominated joint breakages. Such interlocking promotes dilation during shear deformation; however, under confined-stress conditions near the wellbore, dilation is mechanically constrained. This suppression of dilation generates additional normal stress on the near-wellbore region, effectively increasing the local minimum principal stress around the borehole, as shown in Figure 8. Consequently, tensile fracture initiation is more strongly resisted, requiring higher injection pressure to overcome the elevated confinement and resulting in a delayed, higher breakdown pressure relative to the fractured media of lower NF density (Barton et al., 1985).

The time to break down follows the same trend as the breakdown pressure, with cases exhibiting higher breakdown pressures also requiring longer times to initiate fracture. This also reflects higher effective confinement and shear resistance around the wellbore in the high-density NF case. Consequently, broken joint length decreases with increasing NF density due to weakening of the reservoir model caused by the addition of natural fractures, which limit elastic energy accumulation. A further increase in NF density leads to a delay and even higher breakdown pressures, allowing greater elastic energy storage and release and promoting more extensive post-breakdown fracture propagation. However, higher breakdown pressure in high-density NF model compared to the homogeneous model does not necessarily

translate to longer broken joints. We attribute this to leak off of the injected fluid through the crossed NFs, which leads to the dissipation of part of the input energy through viscous drag mechanism rather than toughness-dominated energy dissipation to create new fractures.

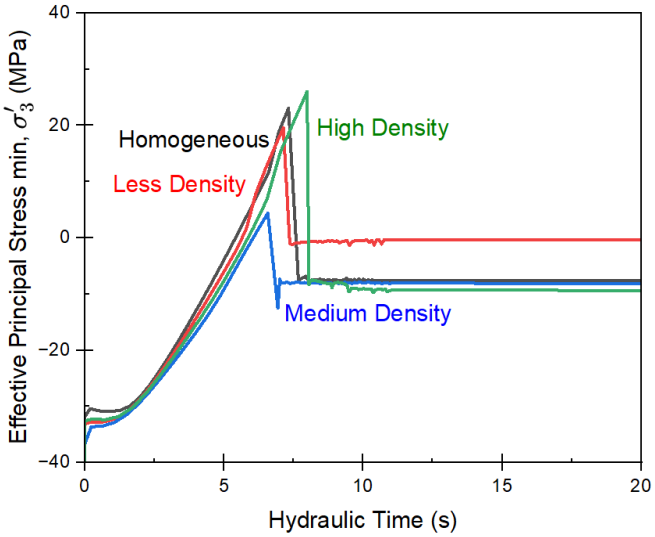

Figure 8: Effective minimum principal stress (σ'$_3$) at the top of the borehole as a function of hydraulic time for homogeneous, low-density, medium-density, and high-density NF cases.

6. CONCLUSIONS

This study provides new insights into wellbore breakdown behavior in homogeneous and naturally fractured media by clarifying the mechanical and hydromechanical mechanisms through which natural fractures influence breakdown pressure, fracture initiation near the wellbore, and fracture network growth. The main conclusion of this study is:

- In lower to moderate density NF formations, reduced confinement and earlier breakdown suggest that lower injection pressures compared to the homogeneous case may be sufficient to initiate fractures, but lead to limited broken joints and reduced stimulation efficiency. This is due to increased rock mass compliance with increasing NF density up to some degree.
- Once NF density exceeds a threshold, rock block interlocking effects leads to elevated effective minimum principal stress around the borehole, generating strong local confinement, higher mobilized pressures at breakdown, and longer time to failure.
- Injection parameters cannot be selected independently of NF density of the target reservoir, as increasing NF density changes the characteristics of the system.

Future work will focus on incorporating natural fracture bond strength and permeability to investigate how fracture mechanical and hydraulic properties jointly control hydromechanical behavior, breakdown pressure, and fracture network evolution in naturally fractured media.

7. ACKNOWLEDGEMENT

This project was supported by the Department of Civil and Environmental Engineering at the University of Utah.

REFERENCES

Barton, N., & Bandis, S. (1982). Effects of block size on the shear behavior of jointed rock. *ARMA US Rock Mechanics/Geomechanics Symposium*, ARMA-82.

Barton, N., Bandis, S., & Bakhtar, K. (1985). Strength, deformation and conductivity coupling of rock joints. *International journal of rock mechanics and mining sciences & geomechanics abstracts*, 22(3), 121-140.

Bijay, K. C., Frash, L. P., Iyare, U. C., Li, W., Madenova, Y., Smith, M., & Kroll, K. (2025). High-Temperature Triaxial Direct Shear Testing for Utah FORGE. *50th Workshop on Geothermal Reservoir Engineering*. Stanford University, Feb. 9-11.

Chen, Z., Jeffrey, R. G., Zhang, X., & Kear, J. (2017). Finite-element simulation of a hydraulic fracture interacting with a natural fracture. *SPE Journal*, 22(01), 219-234.

Chong, Z., Li, X., Chen, X., Zhang, J., & Lu, J. (2017). Numerical investigation into the effect of natural fracture density on hydraulic fracture network propagation. *Energies*, 10(7), 914. MDPI.

Daneshy, A. (2019, January). Three-dimensional analysis of interactions between hydraulic and natural fractures. *SPE Hydraulic Fracturing Technology Conference and Exhibition* (D011S002R003). SPE.

De Pater, C. J., & Beugelsdijk, L. J. L. (2005). Experiments and numerical simulation of hydraulic fracturing in naturally fractured rock. *ARMA US Rock Mechanics/Geomechanics Symposium*, ARMA-05.

Detournay, E. (2004). Propagation regimes of fluid-driven fractures in impermeable rocks. *International Journal of Geomechanics*, 4(1), 35-45.

Geomechanica Inc. (2021). *Irazu 2D Software: Theory Manual*. Toronto, Canada.

Hoek, E., & Brown, E. T. (1980). Empirical strength criterion for rock masses. *Journal of the geotechnical engineering division*, 106(9), 1013-1035.

Huang, L., Liu, J., Zhang, F., Dontsov, E., & Damjanac, B. (2019). Exploring the influence of rock inherent heterogeneity and grain size on hydraulic fracturing using discrete element modeling. *International Journal of Solids and Structures*, 176, 207-220.

Hubbert, M. K., & Willis, D. G. (1957). Mechanics of hydraulic fracturing. *Transactions of the AIME*, 210(01), 153-168.

Kolawole, O., & Ispas, I. (2020). Interaction between hydraulic fractures and natural fractures: current status and prospective directions. *Journal of Petroleum Exploration and Production Technology*, 10(4), 1613–1634. Springer.

Kwok, C. Y., Duan, K., & Pierce, M. (2020). Modeling hydraulic fracturing in jointed shale formation with the use of fully coupled discrete element method. *Acta Geotechnica*, 15(1), 245-264.

Lecampion, B. (2009). An extended finite element method for hydraulic fracture problems. *Communications in Numerical Methods in Engineering*, 25(2), 121-133.

Lisjak, A., Kaifosh, P., He, L., Tatone, B. S. A., Mahabadi, O. K., & Grasselli, G. (2017). A 2D, fully-coupled, hydro-mechanical, FDEM formulation for modelling fracturing processes in discontinuous, porous rock masses. *Computers and Geotechnics*, 81, 1-18.

Lisjak, A., Tatone, B. S., Mahabadi, O. K., Grasselli, G., Marschall, P., Lanyon, G. W., ... & Nussbaum, C. (2016). Hybrid finite-discrete element simulation of the EDZ formation and mechanical sealing process around a microtunnel in Opalinus Clay. *Journal of Rock Mechanics and Rock Engineering*, 49, 1849-1873.

Mahabadi, O. K., Lisjak, A., Munjiza, A., & Grasselli, G. (2012). Y-Geo: new combined finite-discrete element numerical code for geomechanical applications. *International Journal of Geomechanics*, 12(6), 676-688.

McLennan, J. (2022). Utah FORGE Well 16A (78)-32 Stimulation Data (April). *USDOE Geothermal Data Repository*; Energy and Geoscience Institute.

Munjiza, A., & Andrews, K. R. F. (1998). NBS contact detection algorithm for bodies of similar size. *International Journal for Numerical Methods in Engineering*, 43(1), 131-149.

Potyondy, D. and Cundall, P. (2004). A bonded-particle model for rock, *International Journal of Rock Mechanics and Mining Sciences*, 41(8), 1329-1364.

Roshankhah, S., Nejad, A. K., Teran, O., & Mohammadi, K. (2020). Modelling the variation in the behaviour of pre-fractured rocks subjected to hydraulic fracturing with permeability of the rock matrix using finite-discrete element method. *2nd International Conference on Energy Geotechnics*, Vol. 205, p. 08001, EDP Sciences.

Shandilayaa, S., Alaleelib, M., Kim, S.H., Mobasher, M., and Roshankhah, S. (2026). Local Stress Redistribution Controls Interactions between Hydraulic Fractures and Pre-existing Fractures. Under Review in the *International Journal of Rock Mechanics and Mining Sciences*.

Tatone, B. S., & Grasselli, G. (2015). A calibration procedure for two-dimensional laboratory-scale hybrid finite–discrete element simulations. *International Journal of Rock Mechanics and Mining Sciences*, 75, 56-72.

Wangen, M. (2013). Finite element modeling of hydraulic fracturing in 3D. *Computational Geosciences*, 17, 647-659.

Wasantha, P. L. P., Konietzky, H., Xu, C. (2019). Effect of in-situ stress contrast on fracture containment during single-and multi-stage hydraulic fracturing. *Engineering Fracture Mechanics*, 205, 175-189.

Xing, P., Damjanac, B., Moore, J., & McLennan, J. (2022). Flowback test analyses at the Utah Frontier Observatory for Research in Geothermal Energy (FORGE) site. *Journal of Rock Mechanics and Rock Engineering*, 55(5), 3023–3040. Springer.

Yan, C., Xie, X., Ren, Y., Ke, W., & Wang, G. (2022). A FDEM-based 2D coupled thermal-hydro-mechanical model for multiphysical simulation of rock fracturing. *International Journal of Rock Mechanics and Mining Sciences*, 149, 104964.

Yan, C., Zheng, H., Sun, G., & Ge, X. (2016). Combined finite-discrete element method for simulation of hydraulic fracturing. *Journal of Rock Mechanics and Rock Engineering*, 49(4), 1389-1410.

Zhao, F., Shi, Z., Yu, S., & Zheng, H. (2023). A review of fracture mechanic behaviors of rocks containing various defects. *Underground Space*.

Zheng, H., Pu, C., & Sun, C. (2020). Numerical investigation on the hydraulic fracture propagation based on combined finite-discrete element method. *Journal of Structural Geology*, 130, 103926.